

Retraction

Retracted: Experimental Study on the Principle of Oxygenation and Oxygenation Performance of Surface Blade Aerator

Advances in Materials Science and Engineering

Received 26 December 2023; Accepted 26 December 2023; Published 29 December 2023

Copyright © 2023 Advances in Materials Science and Engineering. This is an open access article distributed under the Creative Commons Attribution License, which permits unrestricted use, distribution, and reproduction in any medium, provided the original work is properly cited.

This article has been retracted by Hindawi, as publisher, following an investigation undertaken by the publisher [1]. This investigation has uncovered evidence of systematic manipulation of the publication and peer-review process. We cannot, therefore, vouch for the reliability or integrity of this article.

Please note that this notice is intended solely to alert readers that the peer-review process of this article has been compromised.

Wiley and Hindawi regret that the usual quality checks did not identify these issues before publication and have since put additional measures in place to safeguard research integrity.

We wish to credit our Research Integrity and Research Publishing teams and anonymous and named external researchers and research integrity experts for contributing to this investigation.

The corresponding author, as the representative of all authors, has been given the opportunity to register their agreement or disagreement to this retraction. We have kept a record of any response received.

References

- [1] P. Xing, C. Yu, K. Li, and H. Wu, "Experimental Study on the Principle of Oxygenation and Oxygenation Performance of Surface Blade Aerator," *Advances in Materials Science and Engineering*, vol. 2022, Article ID 3518833, 14 pages, 2022.

Research Article

Experimental Study on the Principle of Oxygenation and Oxygenation Performance of Surface Blade Aerator

Pu Xing , **Chen Yu**, **Kangkang Li**, and **Hui Wu**

Nanchang Hangkong University, 696 Fenghe South Avenue, Nanchang, China

Correspondence should be addressed to Pu Xing; xingpu@nchu.edu.cn

Received 29 December 2021; Revised 4 February 2022; Accepted 14 February 2022; Published 16 March 2022

Academic Editor: Palanivel Velmurugan

Copyright © 2022 Pu Xing et al. This is an open access article distributed under the Creative Commons Attribution License, which permits unrestricted use, distribution, and reproduction in any medium, provided the original work is properly cited.

In this article, the principle of aeration of aerator is analyzed through CFD simulation analysis and high-speed camera observation of aerator blades. Firstly, the flow field of oxidation ditch under the influence of a new curved blade aerator is simulated and analyzed. Then, the oxygenation performance of aerator under different operating parameters, that is different immersion depth and speed, is experimentally studied, and the structural optimization design of blade is carried out. Finally, the best parameters affecting oxygenation dynamic efficiency are obtained by fitting the experimental data, which provides a reference for the further optimization design of the aerator.

1. Introduction

The shortage of water resources and water pollution are worldwide problems. The discharge of wastewater remains high, and the water environment needs to be improved urgently. As a highly competitive secondary biological treatment technology in urban sewage and industrial wastewater treatment, oxidation ditch treatment process has the characteristics of simple process, good effluent quality, and easy stability of sludge [1] and has been widely used all over the world [2]. As the main equipment in the oxygen aeration link in the oxidation ditch [3], the aerator determines the treatment efficiency, energy consumption, and stability of the oxidation ditch, especially suitable for Carousel oxidation ditch [4]. The inverted umbrella aerator has the advantages of simple structure, strong oxygenation capacity, and high power efficiency [5], which is widely used in the surface aeration link of sewage treatment plant.

At present, there is a contradiction between oxygen charging, flow pushing, and energy consumption in the work of inverted umbrella aerator. The blade installation angle, blade number and blade design of inverted umbrella aerator, the rotating speed of aerator, and the immersion depth of impeller all have a certain impact on the

oxygenation performance. Scholars at home and abroad have also conducted a series of studies on these factors [6–8].

Wang Jiaquan [9] simulated the working conditions and oxygenation performance of various inverted umbrella aerators and analyzed the effects of blade installation angle, blade number, and blade shape on oxygenation capacity. Liu Jiawei [10] built an inverted umbrella aerator test-bed to analyze the flow characteristics of the internal flow field of the oxidation ditch under different motion parameters. The response surface method model was established to optimize the performance of the aerator. C Beatriz combined different rotating speeds, immersion depth, and blade angle and obtained the equation for estimating the performance of aerator through dimensional analysis [11]. Wei Wenli used RNG $k-\epsilon$ turbulence model in CFD software and multi-reference system method are used to analyze the distribution characteristics of overall gas content distribution rate and flow field characteristics in the stirred tank [12]. Wang Y studied the oxygenation performance of aerator under different rotating speed, immersion depth, and liquid level [13]. Dong L found that at the same speed, the oxygen charging speed of oxidation ditch will slow down with the increase of operation time [14]. Ming J studied the performance of aerators with different blade shapes [15].

Different from the straight plate blades of the traditional inverted umbrella aerator, Xing Pu and others studied and designed an aerator with curved blades, and the blade profile is designed according to the law of logarithmic helix [16, 17]. Through the finite element analysis of the aerator blade, and according to the real flow field, a series of optimization of the aerator blade is carried out to make it have better oxidation and aeration performance.

2. Mathematical Simulation Experiment

2.1. Modeling and Meshing. First of all, using SOLIDWORKS software to model the aeration wheel and oxidation ditch, the aerator impeller has a maximum diameter of 90 mm, the height is 25 mm, the number of blades is 6, the blade inclination angle is 70° , and the middle opening diameter is 50 mm. Curve blades are controlled by a trolling helix, which is built by the software's equation-driven curve, as shown in equation (1), and then the blade is generated by scanning, as shown in Figure 1.

$$\begin{cases} x(\theta) = r \cdot e^{\theta/\tan \beta} \cdot \cos \theta \\ y(\theta) = r \cdot e^{\theta/\tan \beta} \cdot \sin \theta \end{cases} \quad (1)$$

where r is the initial polar diameter, θ is the spiral rotation angle, and β is the helix angle.

After the construction of the aerator impeller model is completed, the working area of the aerator needs to be established, and this simulation uses the oxidation ditch model during the experiment. After modeling, the model is assembled, as shown in Figure 2, which is 1000 mm long and 800 mm wide. Then the origin of the coordinate system is placed at the center of the surface on the aerator impeller, which is 300 mm away from the bottom of the barrel.

The processed model is then imported into ANSYS, the grid is divided using the fluent meshing feature, and the maximum mesh size of the stationary domain is set to 7 mm, rotating the domain. The maximum mesh size is set to 4 mm. The final generated total number of grids is 2.71million, the three rotating domain grids are 40,000, the mass is 0.5 or more. The number of static domain grids is 2.59 million, with a mass of more than 0.8, which meets the grid quality requirements required for calculation. A grid-dividing diagram of the rotation and stationary fields is shown in Figure 3.

2.2. Numerical Simulation Analysis. The flow situation in the oxidation ditch is more complex; it takes a certain amount of time from the start of the aerator to the stable state of the oxidation ditch flow field, and the distribution of the flow field is very different at different times before the stabilization of the same channel, so the flow field is analyzed after the oxidation ditch is selected to reach a stable state. To facilitate the description of the various areas in the oxidation ditch, three aerator impellers are named with four ramps, as shown in Figure 4. In the vertical direction, the oxidation ditch flow field is divided into upper, middle, and lower layers. Four runs and three impellers were named, and the

walls of each channel was placed on and off the walls to distinguish them.

In order to analyze the flow field in the oxidation ditch, the simulation results are processed by CDF-post software, and the velocity cloud map, flow map, and turbulent kinetic energy cloud map at different locations in the flow field are made.

Figure 5 shows turbulent kinetic energy cloud maps of impellers 2 and 3 in the oxidation ditch at the XZ cross section, and Figure 6 shows velocity flow clouds at the impeller sections 2 and 3, where 6(a) shows impeller 2.

As can be seen from the two 6(a) diagrams, areas with high turbulence energy (the yellow and red areas in the figure) are distributed near the free liquid surface. According to the two-film theory, the membrane of the two phases of the turbulent local gas fluid becomes thinner and is conducive to the transfer of oxygen. Figure 6(a) have two red areas in the area: one around the blades, the outermost and fastest line of the aerator impeller, the largest relative speed of liquid to air, and the higher intensity of turbulent kinetic energy. The other is where the liquid collides with the wall. From Figure 6(b), it can be seen that the dense flow area is concentrated at the gas-liquid interface near the wall of the oxidation ditch, and there is a circulation vortex in the upper and lower phases of the gas liquid at the wall. Liquids have a higher speed when moving towards the wall, and it will take with the air on the surface and will move upward when it is close to the wall, while the negative pressure generated by blade rotation will cause the air above the impeller to move downwards, so the air above the surface near the wall will produce circulation. Some liquids are hit at the wall and move upward along the wall before falling into the water under the action of gravity, the liquid falling into the water will collide with the liquid moving towards the wall, will form bubbles and vortexes, and the water curtain generated by the water leap will also hit the surface of the water near the wall to form bubbles, so there is strong turbulent motion near the wall. Figure 6 is blade 2, and the left side of the blade is the right side of the wall of the channel; hence the liquid on the left will collide with the wall and the liquid on the right will fall into the flow way, so in Figure 5(a) turbulent kinetic energy distributions are different on the left and right, and there is no significant air circulation in the upper right in Figure 6(a).

Figure 7 are three-dimensional flow maps of the oxidation ditch at different angles when the inflow field reaches a stable state. Figure 8 are velocity cloud maps and velocity maps within oxide ditches at different depths (XY sections) when the flow field is stable, H is the distance of the liquid surface from the bottom of the pool, the aerator impellers move clockwise, the blue area in the figure has the lowest flow rate, the red area has the highest flow rate, and the direction of liquid flow in the oxidation ditch is shown by the black arrow in the figure.

As can be seen from Figure 7(a), the flow field near the blade has the highest speed, and the liquid leaves the impeller at a velocity perpendicular to the direction of the blade. The liquid pushed by blade 1 enters the a and b channels, and as can be seen from Figures 7 and 8(a), the distance between the

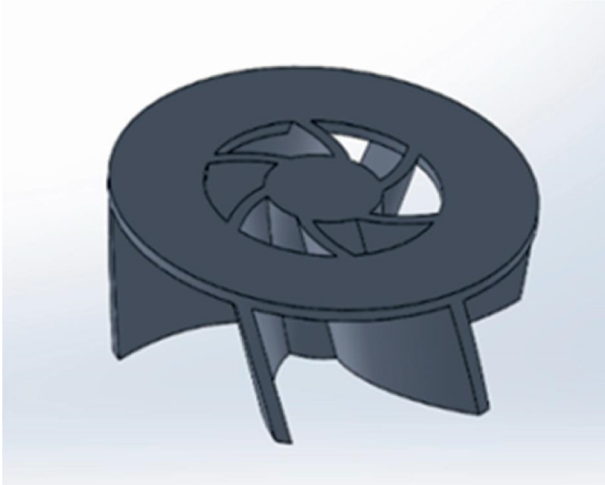


FIGURE 1: Impeller 3D model.

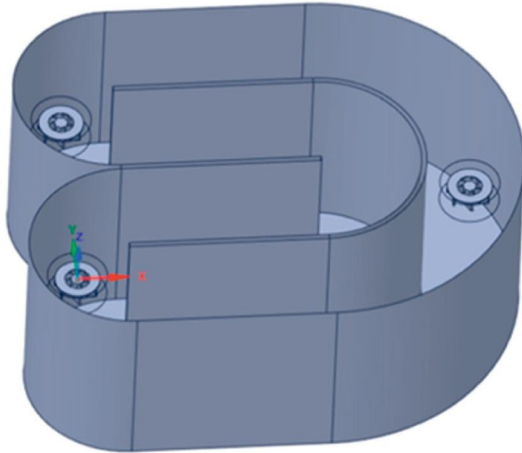


FIGURE 2: 3D model of the oxide ditch.

speed and the line in the b-runway is significantly greater than a, so the b-channel is the main push area of blade 1. Then the main push flow areas of blades 2 and 3 are *d* and *a*, respectively.

The liquid pushed by blades 2 and 3 meets on the right side of the *d*-flow channel, the liquid pushed by blades 1 and 3 meets on the lower left side of the *a*-channel, and the velocity direction changes after the two liquids meet, and the vector map at different depths shows that the liquid flows below its nearest impeller after the intersection. As can be seen from Figure 8(b)–8(d), the fast flow rate of liquid in the mid-flow field is mainly concentrated on the wall of the main push flow area, and the flow rate area gradually away from the corresponding aerator impeller as the depth increases. As can be seen in five images except Figure 8(a), the liquid velocity below the blade is generally moving towards the blade.

Channel *b* is the main push area of blade 1, the direction of liquid velocity is different at different depths, in the stratosphere layer, Figure 8(a) and 8(b), the velocity direction to the right, after contact with the wall at the end of

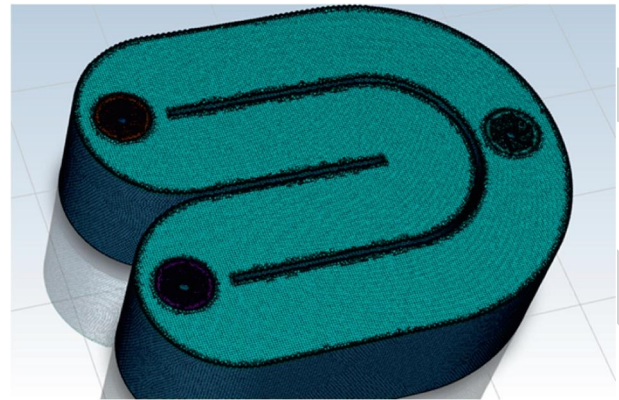


FIGURE 3: Grid division diagram.

the flow way, will flow along the wall facing the flow channel *c*; In Figure 8(c) and 8(d), the velocity of the high-flow area near the wall is directed to the right, but after touching the wall at the end of the flow way, the velocity is divided into two parts: one part continues to flow along the wall towards the flow channel *c*, and the other part flows back to the lower wall flow way of channel *b*. In the lower level of the flow field, in Figure 8(e) and 8(f), the flow rate of the liquid is mainly to the left, as opposed to the upper flow field. As can be seen from Figure 7, (a) circulation phenomenon occurs in runway *b* on a vertical cross section. The flow of channel *d* at different depths is similar to that of flow way *b*, and there is also a circulation in the vertical direction.

The flow at blade 3 is different from that of the other two blades, the main push flow area is the ring flow channel and the *a*-flow channel, the blade-driven liquid will flow down the outer runoff wall of the ring into the *a*-runway. After entering the *a*-channel, the high-speed area is mainly concentrated at the lower wall of the *a*-flow channel, and with the increase of depth, the position of high-flow rate gradually moves to the left, and the flow rate near the wall above the channel is lower. At the upper level of the flow field, the liquid speed is to the left, but there is a low-flow rate zone on the left side of the wall on the *a*-stream, where the liquid will produce a return flow in Figure 8(a). In the middle and lower layers of the *a*-flow channel, the flow rate gap between the upper and lower walls is large, and a circulation is generated between the high-flow zone and the low-flow zone, and the position of the circulation gradually moves to the right with the increase of depth.

The *c*-flow channel is the lowest speed area in the entire oxidation ditch flow field, and the liquid pushed by blade 1 will enter the *c*-flow along the circular wall at the corner, creating a circulation horizontally in the lower right-hand area of the middle of the *c*-flow.

Most of the liquid pushed by blades 7 and 1 enters the *b*-flow channel and creates a vertical circulation in the main push flow area, while the remaining push flow fluid flows downwards after hitting the wall, entering under the impeller and forming a small circulation near the impeller. The flow field near blade 2 is similar to blade 1. The liquid pushed upward by blades 2 and 3 meets at the junction of the *d*-runway and the ring runway, and the two fluids move

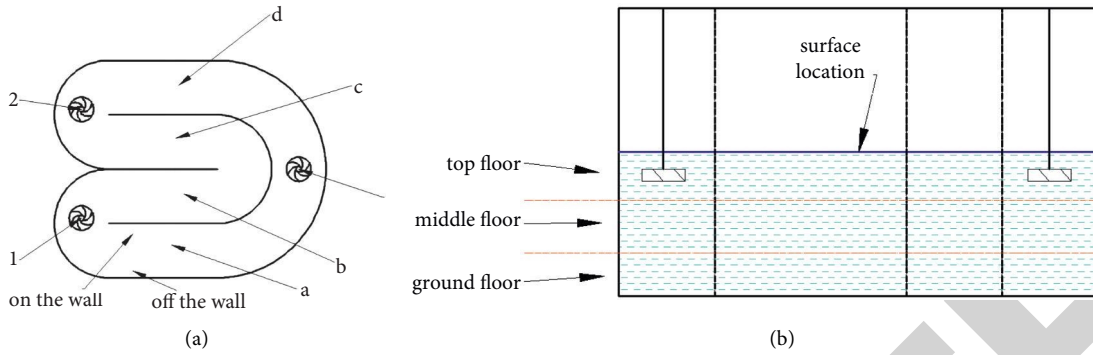


FIGURE 4: The name of the flow field and the flow channel.

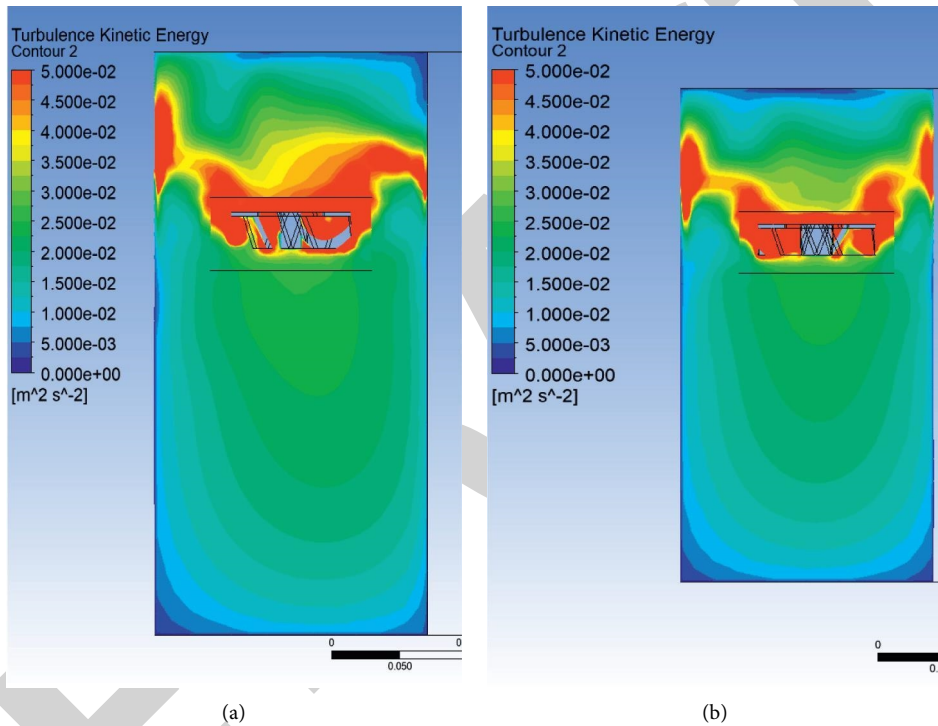


FIGURE 5: Turbulent kinetic energy cloud map.

below blade 3 after the encounter, some of which flows towards the impeller to form a circulation. The liquid pushed down by blade 3 enters the a-runway along the curved wall and eventually moves under blade 1. At the same time, there will be spiral circulation near the wall of the a-channel.

Figure 9 is a turbulent kinetic energy cloud map at different depths when the inflow field of the oxidation ditch is stable. As you can see from Figure 9, places with high turbulence energy (red and yellow areas in the figure) are concentrated around the blades, with low turbulence intensity in each runway. In the figure, H is the position of the section, the bottom of the pool H-0 mm, and the surface of the impeller is 300 mm from the bottom of the oxidation ditch, that is in the position of H-300 mm.

Figure 9(a) is light blue directly above the aerator impeller, where turbulence intensity is low, and there is a green area on the periphery with a high turbulence intensity. The fluid here is in a state where it is thrown out of the impeller and moves upward towards the slope, and is exposed to the wall by a drop in gravity. Liquids have a high-flow rate and are constantly in contact with air. The thrown liquid moves towards the wall layer by layer in a wave shape, which will produce vortices of different sizes. When the air contacts, the waves will be drawn into the air and enter the water to form bubbles. Part of the liquid generated by the hydraulic jump will also fall into the water here, and the impact when entering the water surface will draw in part of the air, resulting in high turbulence intensity. There are several red areas near the wall where the

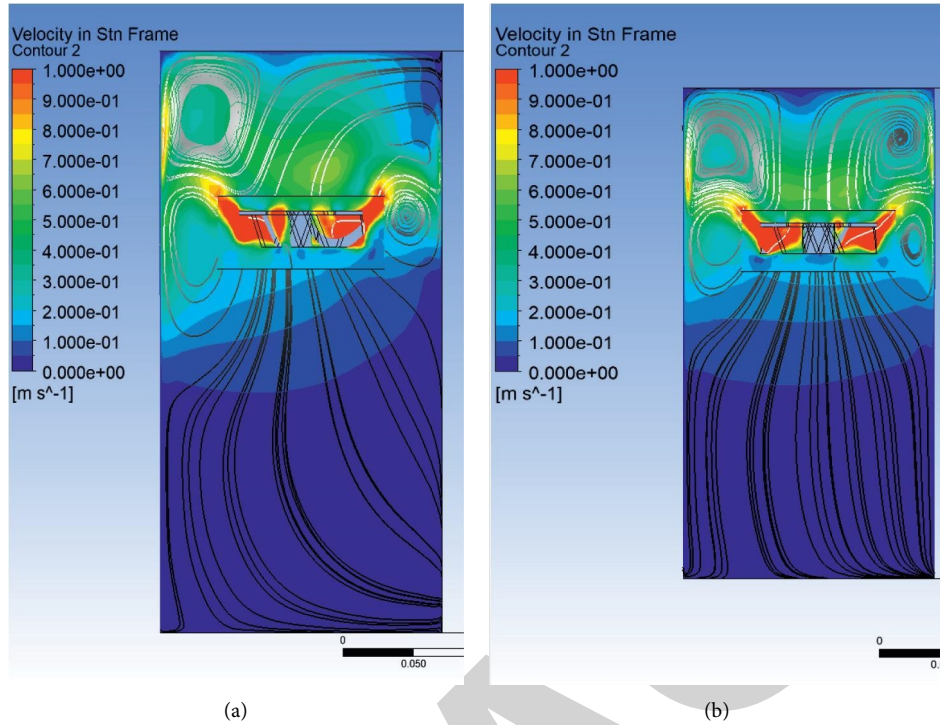


FIGURE 6: Speed stream cloud map.

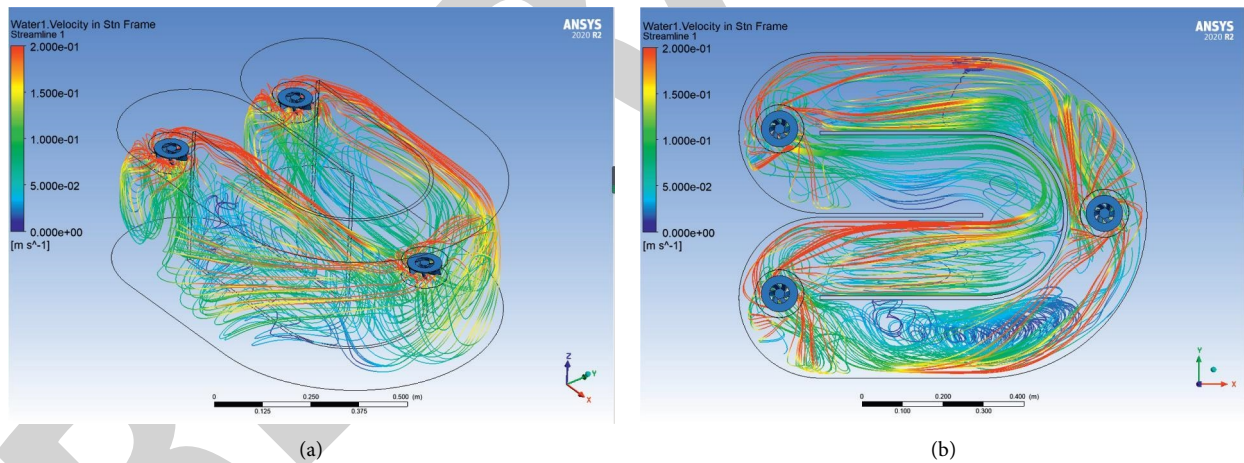


FIGURE 7: Flow charts at different angles.

liquid forms bubbles and moves downwards under the influence of gravity and push currents, where the flow of the liquid changes and has strong turbulent energy. The middle position is a concave structure produced by the high-speed rotation of the aerator impeller, from which air enters near the impeller, with no contact with the liquid surface and low turbulence. At Figure 9(b), the middle area is still a blue low-turbulent kinetic energy region, with a yellow-green ring-shaped high turbulent kinetic energy region on the periphery, and the rest a blue area with general turbulent kinetic energy. The liquid flies out of the yellow-green ring area under the push of the blade, giving it a high turbulence energy. The outer area of the green ring is

below the surface of the water, has no contact with the air, and the turbulence intensity is low.

For the upper and lower parts of the impeller, the area near the blade is the red area with high turbulent energy, and the rest is the cyan area with a certain turbulent kinetic energy (Figures 9(c) and 9(d)). The fluid in the red area with high turbulent kinetic energy is in direct contact with the blade, and the blade continues to work on the liquid. There are a large number of air bag behind the blade, and the relative velocity between the side and tail of the air bag is very fast, accompanied by a large number of bubbles and vortices, which have strong turbulent kinetic energy. The liquid moves upward in the push flow, causing the overall flow rate of the upper part of the blade

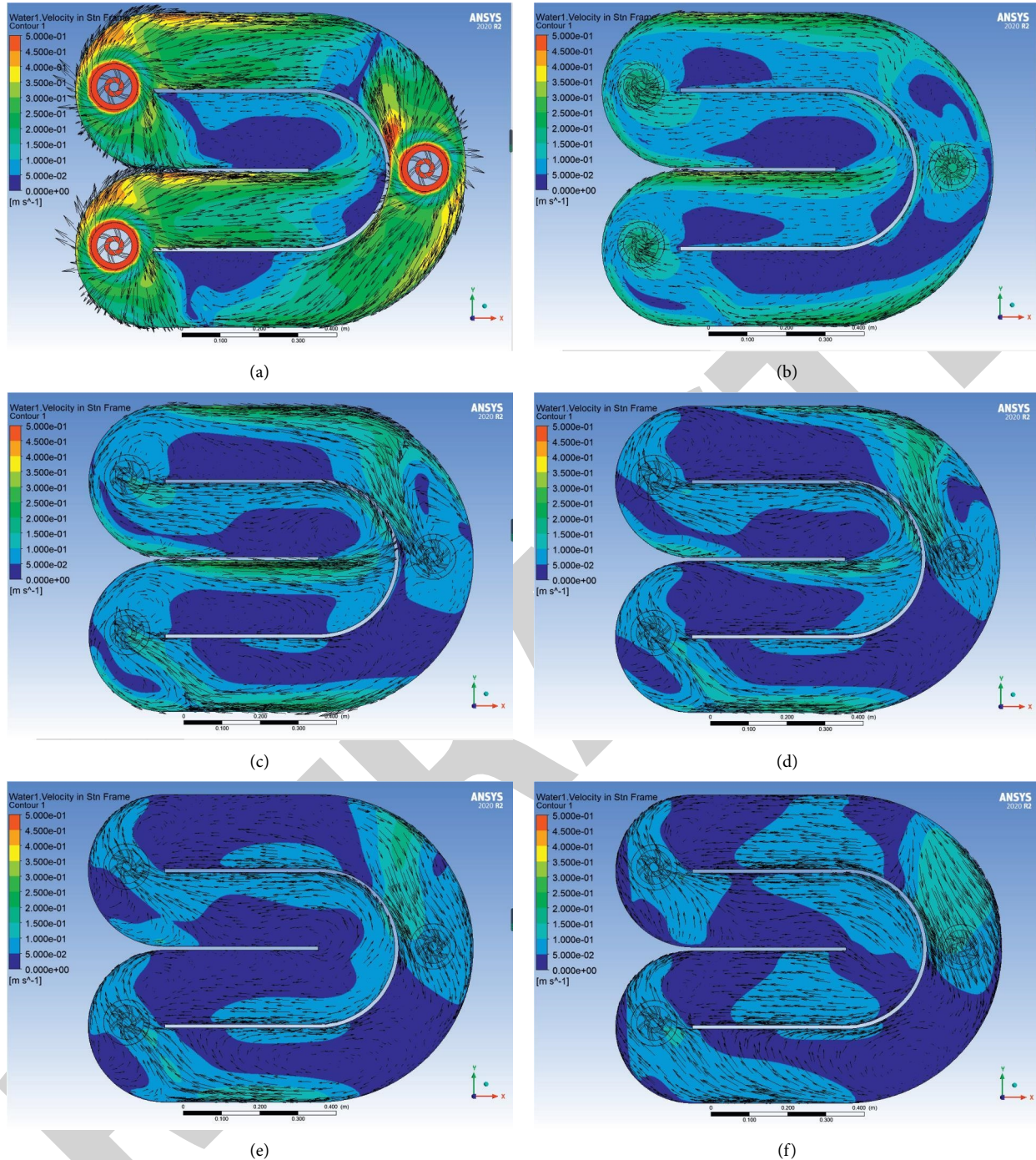


FIGURE 8: Vector and velocity cloud maps at different depths (a) $H = 300$ mm, (b) $H = 250$ mm, (c) $H = 200$ mm, (d) $H = 150$ mm, (e) $H = 100$ mm, and (f) $H = 50$ mm.

to be higher than that of the lower part and the turbulent kinetic energy to be higher than the lower part. For the deep water area below the blade, the red area with high turbulent energy does not appear in the deep flow field, most of the area is cyan, the intensity of turbulence kinetic energy decreases gradually with the increase of depth, especially the area of deep water near the wall (Figures 9(e) and 9(f)). The area with high turbulent kinetic energy is concentrated in the upper layer of the oxidation ditch flow field, in which the fluid will continue to

be pushed by the blade, maintaining the state of high turbulent kinetic energy, and where the oxygen transfer efficiency is high, it appears in the area with strong turbulent dynamic energy.

3. Airbag Characteristic Test

3.1. Experimental Materials and Platforms. In order to study the distribution of airbags during high-speed motion, the flow field near the aerator is photographed by high-speed

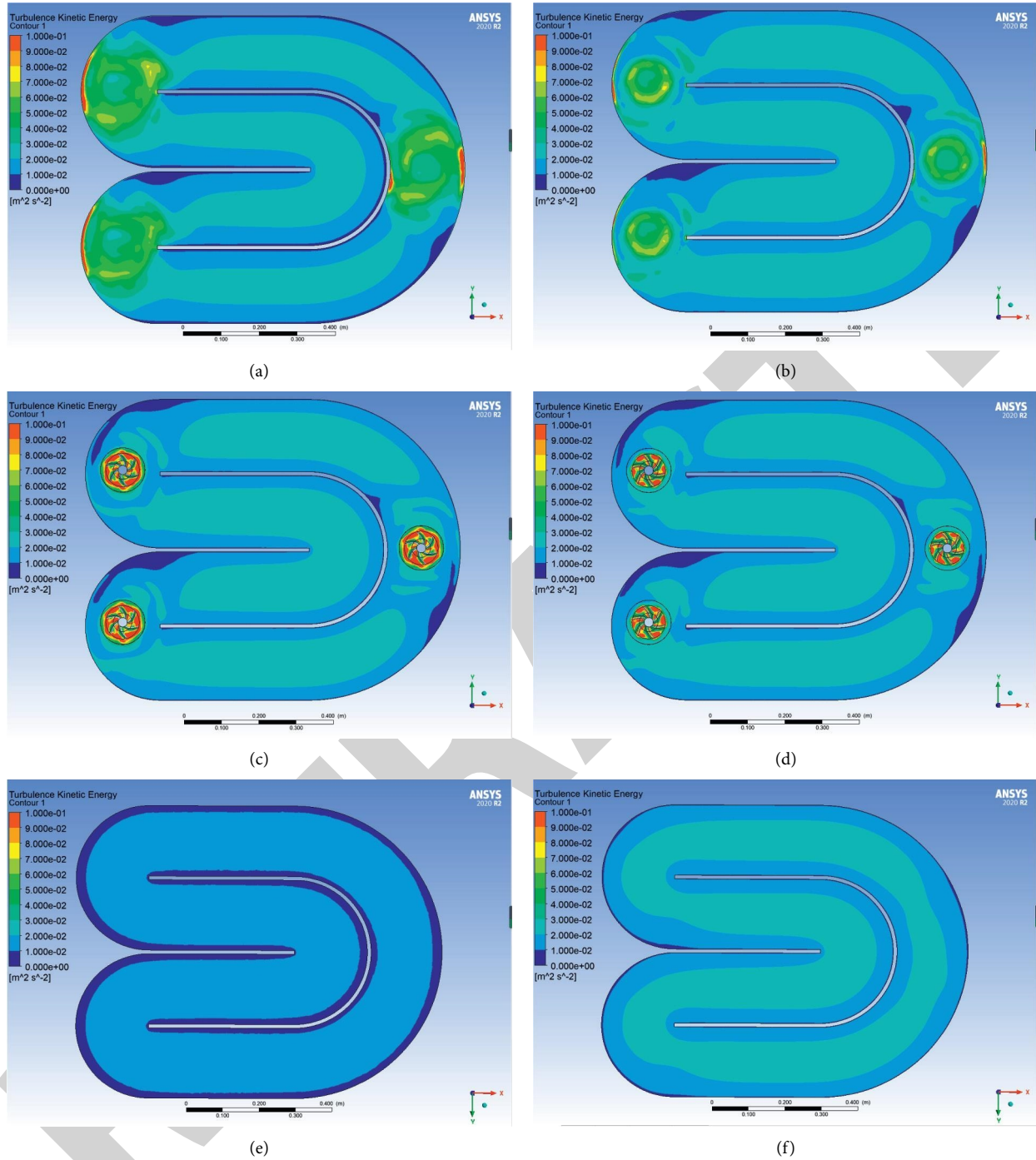


FIGURE 9: Turbulent kinetic energy cloud map at different depths (a) $H = 330$ mm, (b) $H = 310$ mm, (c) $H = 290$ mm, (d) $H = 280$ mm, (e) $H = 200$ mm, and (f) $H = 100$ mm.

camera to observe the situation of bubbles. The equipments used for shooting are Carousel oxidation ditch, curved blade aerator, LED lights, high-speed camera, computer, etc.

The model of the high-speed camera is 5f01. The shooting range selected in the experiment is a square area with a resolution of 840×840 . The set shooting rate is 1000 frames per second and the time of single shooting is 1 second. The high-speed camera and the LED light are shown in Figure 10. A position diagram of the camera and the LED

light at the time of shooting is shown in Figure 11. In Figure 10(a), 1 is an LED lamp, 2 is a high-speed camera, and 3 is a computer for storing data.

In this article, an image processing technique based on distance transformation and watershed algorithm is adopted [18–20]. This technique can be very good at improving noise, background, and bubble adhesion in noninvasive experiments, in order to understand the size distribution of different depth bubbles. The photographed

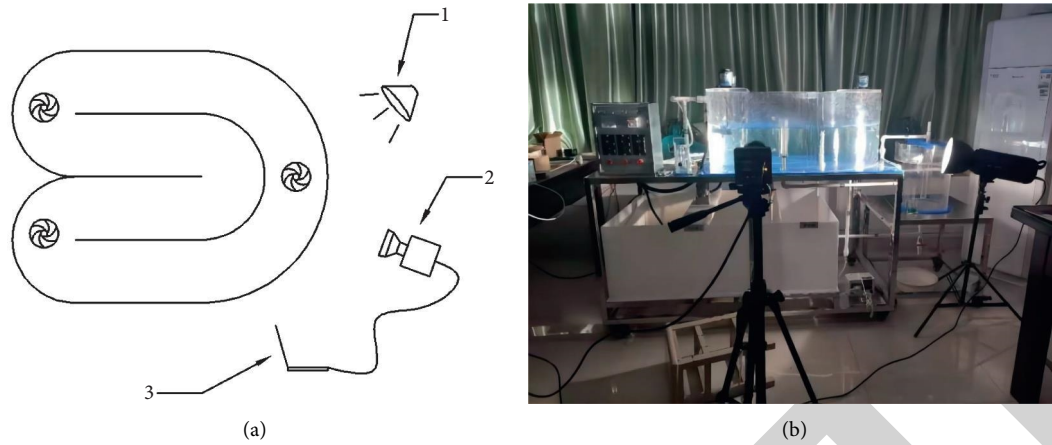


FIGURE 10: High-speed camera with LED lights.

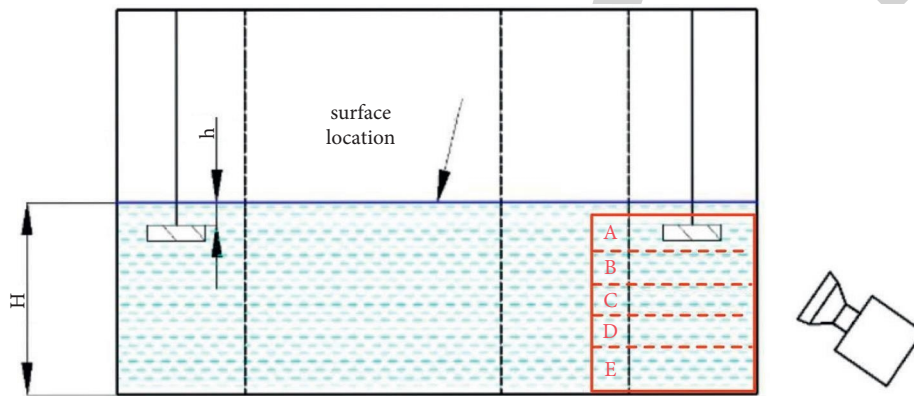


FIGURE 11: High-speed camera with LED and map of the shooting area.

areas are divided into five groups: area A (depth 0 to 60 mm), area B (depth 60 to 120 mm), area C (depth 120 to 180 mm), area D (depth 180 to 240 mm), and area E (depth 240 to 300 mm), and the size distribution of bubbles in each area was identified by image processing technology when the rotational speed was 400 rpm, and the position of the bubbles was photographed as shown in Figure 11. At the same time, for the A-region with the largest number of bubbles, the speed of the aerator is set to 250, 300, 350, 400, and 450 rpm, and the immersion depth is 5, 0, -5, -10, and -15 mm. The size distribution of bubbles in different parameters is observed.

The photos taken are shown in Figure 12. From the figure, we can intuitively see that the shape change of bubbles in the photos is very huge and irregular. This is because the bubbles in the water will collide under the stirring and propulsion of the impeller, resulting in the overlap of bubbles, and the rupture of bubbles is caused by the shear flow effect of eddy current and the instability of bubbles in the water. Due to the above effects, most of the bubbles taken are not spherical or elliptical, and the shape and size change greatly, so we need to deal with the photos.

Through the mean of shift filtering, image binarization, and distance transformation, watershed segmentation is

performed on the image. After watershed segmentation, as can be seen from Figure 13, the phenomena of noise, uneven background, and bubble sticking in the original image have been greatly improved. In the later image analysis, the size, shape, and distribution of bubbles under different rotating speeds and immersion depths should be analyzed.

Next, this article uses the method of equal area circle, and calculates the various dimension parameters of bubbles by the following formula:

$$d_m = \frac{\sum n_L d_L}{\sum n_L}, \quad (2)$$

where d_L is the diameter of the bubble (μm), n_L is the number of bubbles with a d_L diameter, and d_m is the average diameter of the bubble.

Since this experiment uses noninvasive measurements and cannot estimate the volume size of the shooting area, the local gas content is calculated using the picture after the watershed segmentation, as follows:

$$\alpha_g = \frac{S_{\text{bubbles}}}{S_A}, \quad (3)$$

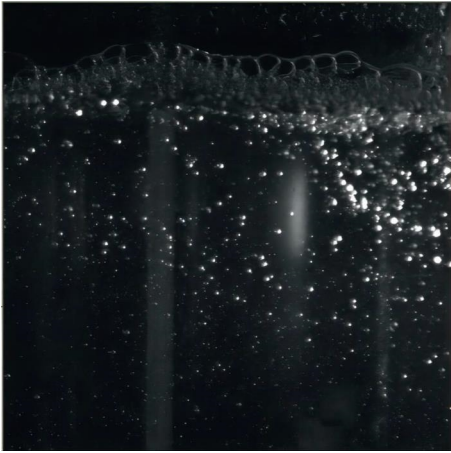


FIGURE 12: Photos taken by high-speed camera.

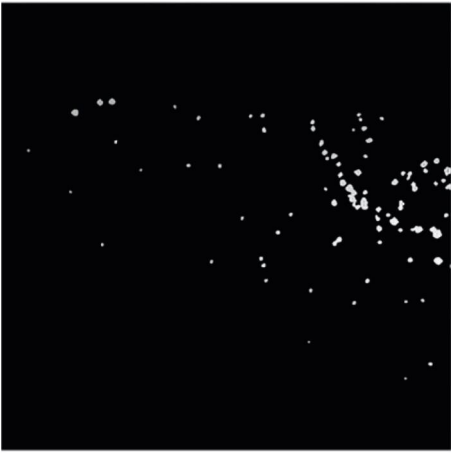


FIGURE 13: Final result of processing.

where α_g is the local gas rate, S_{bubbles} is the total area of the bubble, and S_A is the total area of the shooting area.

3.2. Results and Analysis. Observation of experimental phenomena found that when the impeller rotates at high speed, a large amount of liquid will be thrown from the junction of the blade and the plate to form a water curtain, the water curtain moves obliquely upward, contacts with the air, and finally under the action of gravity falls into the water, called the water leap phenomenon.

Under the pushing action of the blade, the liquid thrown out has a high initial velocity. Under the influence of resistance and gravity, the liquid velocity decreases and begins to fall. At the same time, the liquid disperses from the water curtain into water droplets in the air and finally falls into the water surface. In the process of leaping, the liquid is in full contact with the air and after dispersing into water droplets, the contact area is further expanded. When it falls into the water, it will hit the water surface and wrap a large number of bubbles.

As the impeller rotates at high speed, air enters the airbag behind the blade through the middle opening and perimeter

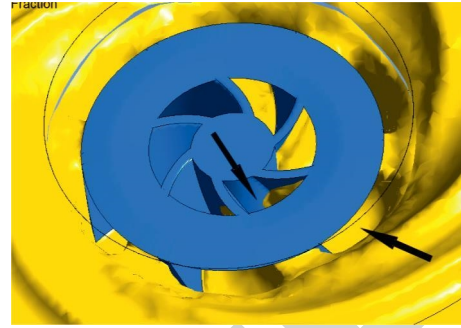


FIGURE 14: Air enters position.

of the impeller, as shown by the black arrow in Figure 14. Airbags increase the area of air–water contact, thereby increasing the rate of oxygen transfer in the aeration machine. Through simulation and high-speed photography, the free surface of the aerator blade from the bottom view is obtained, as shown in Figure 15(a) and 15(b). The distribution of airbags in the two cases in the figure is similar, which shows that the results obtained by numerical simulation have certain accuracy and reference value.

For this purpose, the distribution of airbags on the XY cross section was made, as shown in the flow and velocity vectors of Figure 16. The image shows that the shape of the airbag approximates a trapezoid, naming the surface of the airbag in contact with the rear of the blade as the side of the airbag, and the interface between the airbag and the blade push flow liquid is the back of the airbag. The velocity direction of the liquid and the air entering the air bag are shown in Figure 16(a), and the two phases are in the same speed direction at the back of the airbag, so the turbulent energy here is low. As can be seen from Figure 16(a), water on the side of the airbag is in the opposite direction to air, faster relative to the back, and more frequently exchanged. Observations of high-speed photography show that when the air on the side of the airbag comes into contact with the liquid, bubbles are thrown out of the airbags, which break in the water to form a large number of small bubbles dissolved into the water. This is due to the high-speed movement of the airbags with the blades, the side of the airbags relative to the liquid, as shown in the red area of Figure 17, where the turbulence strength is highest, resulting in more vortex and reflux. As shown by the white arrow in Figure 16(b), 16(a) small vortex forms on the side air–liquid interface of the airbag, and under the action of the vortex, a portion of the air is drawn into the water, forming bubbles of varying sizes. According to the double membrane theory, in the process of oxygen transfer, resistance mainly comes from the membrane of the liquid phase, and the greater turbulence strength can reduce the thickness of the membrane, where the turbulence is strong, the thinner the thickness of the membrane, the higher the efficiency of oxygen transfer.

3.2.1. Distribution of Bubble Size in Different Regions.

The results of watershed treatment show that the maximum size of the bubble is 7 pixels, because each pixel corresponds

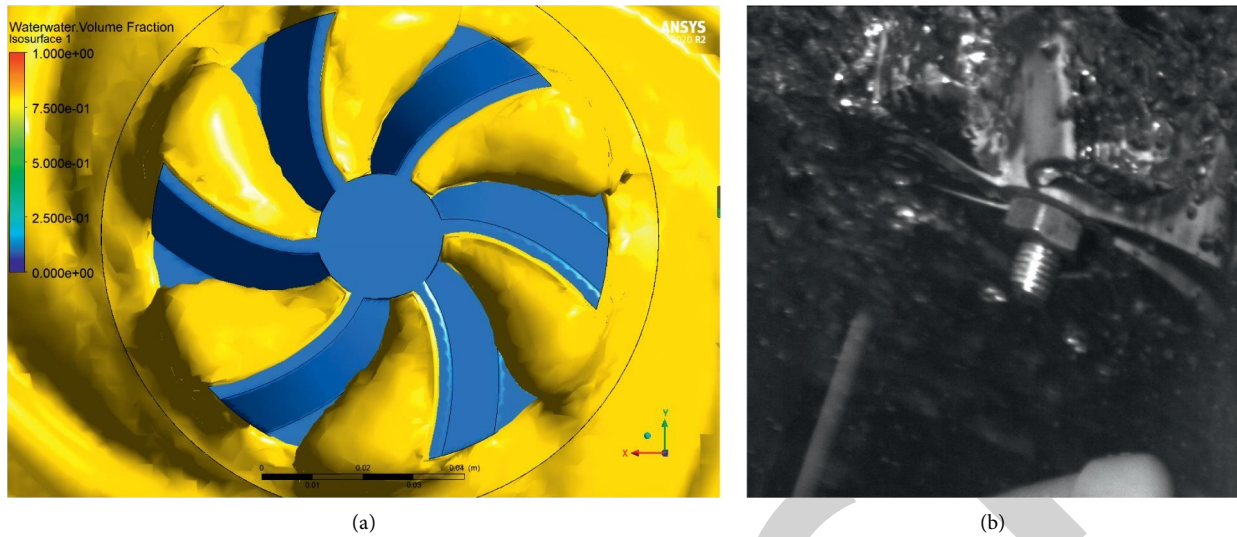


FIGURE 15: Air enters the airbag behind the blade. (a) Air enters position in simulated level. (b) Air enters position in experimental level.

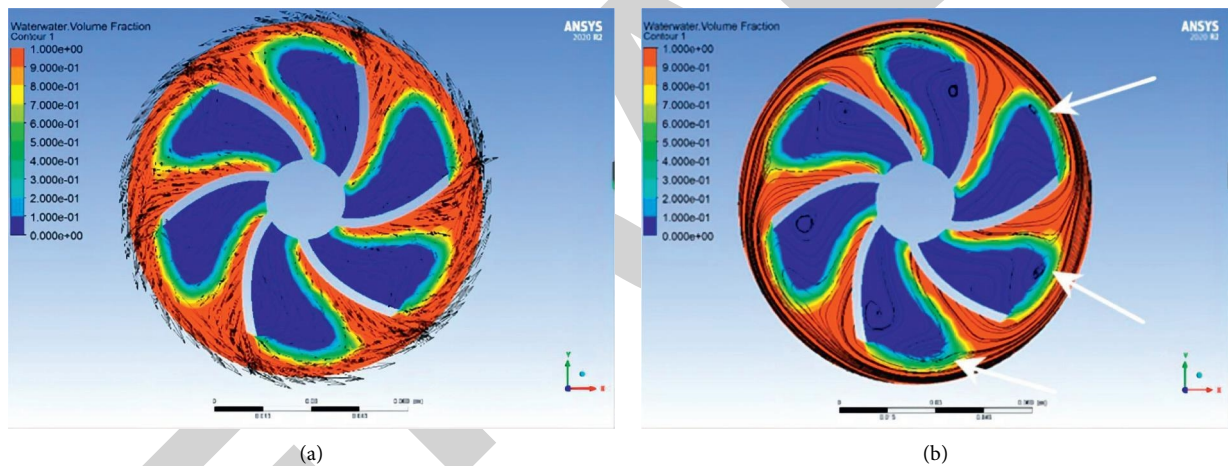


FIGURE 16: Gas-liquid distribution map: (a) Velocity vector and (b) flow chart.

to the size of 0.31 mm, the maximum bubble diameter is 2.17 mm. Bubbles range in size from 0 to 2.17 mm. The size range of bubbles is subdivided into four areas: 0–1.75 pixels, 1.75–3.5 pixels, 3.5–5.25 pixels, and 5.25–7 pixels. The corresponding dimensions are 0–0.54 mm, 0.55–1.09 mm, 1.1–1.63 mm, and 1.64–2.17 mm. The following image (Figure 18) shows the number and size distribution of bubbles in five areas at a speed of 400 rpm and a blade immersion depth of -10 mm.

From Figure 18, it can be seen that from area A to area E, as the depth increases, the number of bubbles decreases gradually, the blade's push flow capacity on the surface of the water body is significantly stronger, and the water leap phenomenon on the surface of the water body will also increase the number of bubbles.

To examine the average bubble size, combined with the results of the high-speed camera, 100 photos were taken in each area to calculate the average bubble size. As can be seen

from Table 1, with the increase of depth, the average size of bubbles gradually decreases, the maximum average size of bubbles is A, and then we set the speed of the aerator to 250, 300, 350, 400, and 450 rpm. The following two situations are then analyzed.

3.2.2. The Size Distribution of Bubbles at Different Speeds and Immersion Depths. The size distribution of bubbles in different parameters is observed. First, immersion depth is set to -10 mm. As can be seen from Figure 19, with the increase of speed, the average size of bubbles gradually increases, when the speed increases from 250 rpm to 350 rpm, the average size of bubbles increases the most. The proportion of bubbles of different sizes at different speeds is: 0–0.54 mm accounting for 26%–67%, 0.55–1.09 mm accounting for 20%–54%, 1.1–1.63 mm accounted for 11%–19%, and 1.64–2.17 mm accounted for 5%–9%. As the speed increases,

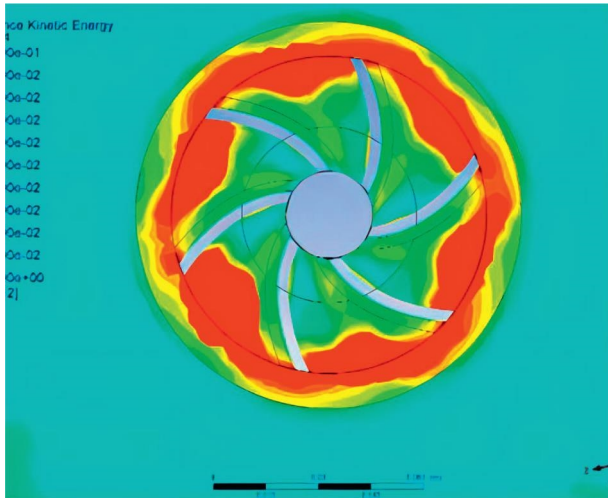


FIGURE 17: Turbulent kinetic energy cloud map.

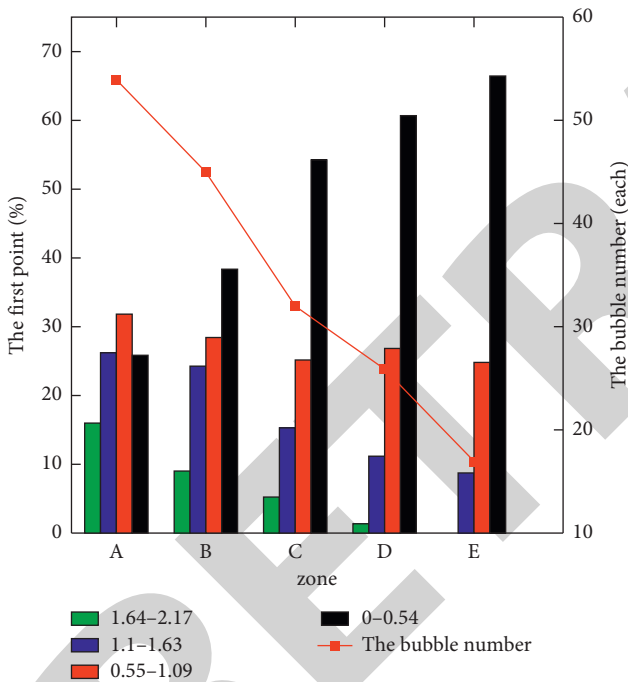


FIGURE 18: Distribution of the number and size of bubbles in each region.

TABLE 1: The size distribution of bubbles in different regions.

Region	Bubble average size/mm	Number of bubbles/each
A	1.56	67
B	1.23	53
C	0.82	32
D	0.76	26
E	0.43	12

the percentage of large bubbles increases gradually, but at speed above 400 rpm, the percentage of large bubbles above 1.1 mm decreases slightly because the atmospheric bubbles break faster due to intense agitation at ultra-high speeds.

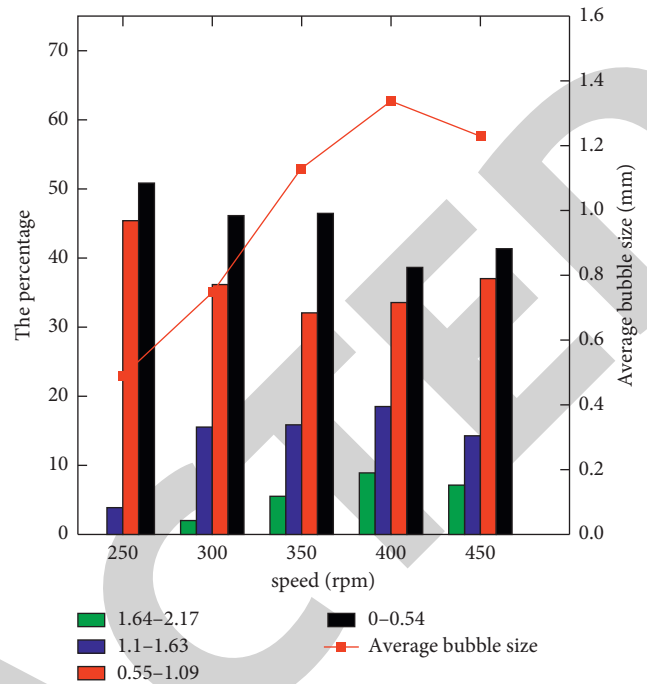


FIGURE 19: The size distribution of bubbles at different speeds.

Next, according to the experimental results of the single-factor experiment, the aerator speed is set to an optimum value of 400 rpm. As can be seen from Table 2, as the depth of immersion increases, the average diameter of the bubbles increases and decreases, reaching a maximum value of -10 mm.

3.2.3. Effect of Different Speeds and Immersion Depth on Local Gas Content. The local gas content of the whole viewfinder range is measured, and the change in local gas content under different environmental parameters is observed. It can be seen from Figure 20 that with the increase of the speed of the aerator, the local gas holdup in area A increases significantly. The reason is that the increase of rotating speed will increase the turbulence intensity at the liquid level and more air will be sucked into the opening of the aerator, and the increase of liquid level flow velocity caused by the increase of rotating speed will also make more bubbles moving to deeper positions and increase the overall gas holdup. With the increase of the immersion depth of the aerator blade, the local gas content of the A area increases first and decreases, with a peak of 0.41% at -10 mm.

3.2.4. Effects of Different Rotating Speed and Immersion Depth on Oxygenation Performance. By adjusting the amount of water in the oxidation ditch, the experimental water surface is selected to be 15 mm, 10 mm, and 5 mm higher than the impeller (record as -15 mm, -10 mm, -5 mm), level with the impeller (0 mm), and 5 mm lower than the impeller. By controlling the motor, the aeration performance of the aerator at 250r/min, 300r/min, 350r/min, 400r/min, and 450r/min was measured. The

TABLE 2: Distribution of bubble size at different immersion depths.

Blade immersion depth/mm	Average bubble diameter/mm	Number of bubbles/each
5	1.19	179
0	1.25	176
-5	1.38	203
-10	1.43	214
-15	1.32	197

TABLE 3: Standard dynamic efficiency SAE under different motion parameters.

Rotation rate(r/min)	Immersion depth(mm)				
	-5	0	5	10	15
250	8.358741	9.903545	10.08076	6.224943	4.407669
300	11.52945	15.61059	19.26355	18.94075	15.92139
350	17.97342	24.30924	30.77573	39.48686	29.99074
400	18.96033	28.60427	37.00992	43.84839	37.47218
450	19.07107	29.24774	36.60363	42.97512	40.83162

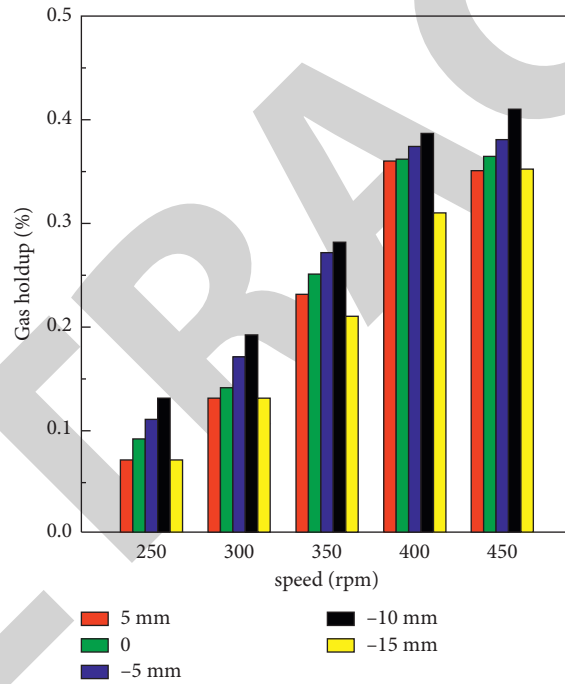


FIGURE 20: Comparison of local gas content at different speeds and immersion depths.

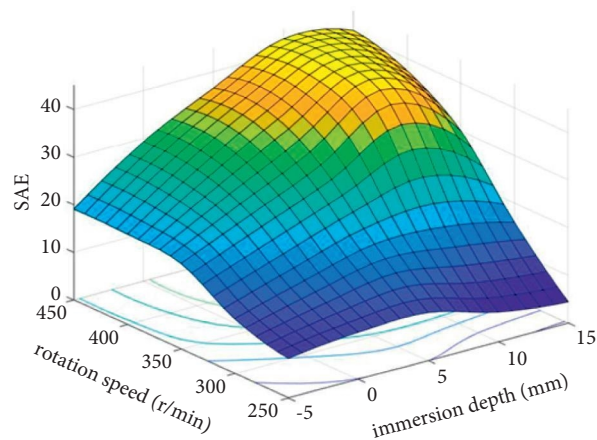


FIGURE 21: Standard power efficiency SAE.

experimental data eliminate the influence caused by the temperature difference in different experiments, and fit the aeration capacity of the aerator under different immersion depth and rotating speed. The standard dynamic efficiency SAE obtained is shown in Table 3. According to Table 3, the curved surface diagram of standard dynamic efficiency SAE under different motion parameters is drawn, as shown in Figure 21.

In Figure 21, the x -axis represents the immersion depth, the y -axis represents the speed, and the z -axis represents the standard dynamic efficiency (mg/min-w). As can be seen from the three-dimensional curved surface diagram, the standard dynamic efficiency of the aerator mainly presents a peak shape. When the immersion depth is 15 mm and the rotating speed is 250r/min, the standard dynamic efficiency of the aerator is the lowest. When the speed of the aerator is lower than 300r/min, the standard dynamic efficiency of the aerator and the dynamic efficiency of the aerator are always at a low level. At this time, changing the immersion depth has no great impact on the standard dynamic efficiency of the aerator. When the speed of the aerator is 400R/min and the immersion depth is about 10 mm, the standard dynamic efficiency of the aerator is the highest.

4. Conclusion

In this article, the motion of the high-speed rotation of the aerator impeller in the oxidation ditch is observed and simulated by fluent simulation and high-speed photography experiments. The flow of liquid after the stabilization of the flow field in the oxidation ditch was analyzed by the VOF free liquid surface model and the Euler multiphase flow model:

- (i) The flow rate and turbulent kinetic energy intensity of the liquid near the surface of the water is higher than that of the water surface, and the horizontal effect of the blade push flow on the inner flow field of the oxidation ditch is greater than the vertical effect. Where turbulence is high, it is around the blade, and where the liquid is flowing fast, it is mainly near the blade.
- (ii) The upper flow field of the flow channel has the highest flow rate near the wall. The liquid of the upper layer of the oxidation ditch flows in the direction of the main push flow of the blade, and the flow rate gap between the upper and lower stratospheres in the main push flow area is large, which will produce circulation in the vertical direction. Most of the liquid in the lower layer of the oxidation ditch flows towards the nearest impeller. At the same time, when the flow rate gap between the two walls of each channel is too large, a return flow is generated in the horizontal direction.
- (iii) The aeration turbine will have a certain lifting ability and push flow ability of the liquid, the liquid under the action of lifting force from the liquid under the blade will move in the direction of the impeller.

After entering the impeller, under the push of the blade, with the blade line movement, a part of the liquid under the combined force of the blade side along the slope, forming a water leap.

- (iv) High-speed rotation around the blade will produce a certain amount of negative pressure, so that the oxidation ditch center fluid facing the depression, air into the rear of the blade to form an air bag, the liquid around the blade flow rate is very fast, forming a turbulent vortex on the contact surface between the liquid and the air bag, and the air will form bubbles and be drawn into the water under the action of turbulence.
- (v) By observing the bubble size, it can be seen that when the rotating speed is 400 rmp and the immersion depth is -10 mm, the bubble size is the largest, and at this depth, the local gas holdup in area A is the largest. In conclusion, the new curved blade aerator has the best oxygenation performance when the rotating speed is 400 rmp, and the immersion depth is -10 mm.

Data Availability

Data sharing is not applicable to this article as no datasets were generated or analyzed during the current study.

Conflicts of Interest

The authors declare that they have no conflicts of interest.

Acknowledgments

The research work of this article was supposed by the China national founding of 51768045, and Technology Plan key R and D Project of Jiangxi province, China (nos. 20181ACG70024 and 20202BBF63010).

References

- [1] A. Zhao and X. Shi, "Comparative analysis and regulation of process design between surface aeration oxidation ditch and bottom aeration biological tank," *Journal of Jiaozuo University*, vol. 35, no. 2, pp. 102–105, 2021.
- [2] S. Fu, X. Lu, and T. Yang, "Development and practice of integrated oxidation ditch a \sim 2/O process water treatment experimental device," *Comprehensive utilization of resources in China*, vol. 39, no. 10, pp. 70–73, 2021.
- [3] Z. Han, S. Li, G. Zhu, Y. Lu, G. Yan, and Z. Li, "Study on the influence factors of oxygen transfer in aeration tanks in highland areas," *Water treatment technology*, vol. 47, no. 6, pp. 34–38, 2021.
- [4] K. Wang, L. Guo, H. Yu, and B. Liu, "Engineering application research of the improved carousel oxidation groove process in PTA wastewater treatment," *Chemical Engineering and Equipment*, vol. 92, no. 11, pp. 255–257, 2017.
- [5] H. Liu, H. Shang, X. Tang et al., "Study on the effect of the number of blades on the aeration performance of the parachute aerator," *Journal of Drainage and Irrigation Mechanical Engineering*, vol. 38, no. 9, pp. 922–927, 2020.

- [6] L. I. Lei, H. E. Jian Jing, and F. Qian, "Numerical simulation of guide plate influence on flow field in the oxidation ditch," *Environmental Science and Technology*, vol. 37, no. 2, pp. 149–154, 2014.
- [7] Z. L. Chen and R. W. Yang, "Effect of eccentric position of guide wall on oxidation ditch performance," *Journal environmental science & technology*, vol. 33, no. 10, pp. 162–165, 2010.
- [8] X. Zhao, *Research on the Technology of Upgrading and Upgrading the Oxide Ditches of Sewage Plants in Small Towns*, Chongqing University, Chongqing, China, 2015.
- [9] Z. Pan, J. Wang, and K. Fan, "Oxygenation performance of several inverted umbrella surface aerators," *Journal of Environmental Engineering*, vol. 6, pp. 180–184, 2012.
- [10] L. Jiawei, *Study on Gas-Liquid Two-phase Flow Mechanism and Optimal Design in Inverted Umbrella Aerator [D]*, Jiangsu university, no. 6, Jiangsu, China, 2019.
- [11] C. Beatriz, R. Pedro, and R. Manfred, "Design of high efficiency surface aerators - Part 1. Development of new rotors for surface aerators," *Aquacultural Engineering*, vol. 31, no. 1-2, pp. 83–88, 2004.
- [12] W. Wenli, W. Lou, and P. Li, "Simulation of gas-liquid two-phase flow in inverted umbrella surface aeration stirred tank," *Journal of System Simulation*, vol. 4, pp. 696–701, 2019.
- [13] Y. Wang, J. Ming, and L. Dong, "Experiment on influence of operating parameters on aeration performance in inverse umbrella aerator," *Transactions of the Chinese Society of Agricultural Engineering*, vol. 33, no. 20, pp. 67–73, 2017.
- [14] L. Dong, Y. Wang, C. Dai, H. Liu, and J. Ming, "Prediction of aeration performance for inverted umbrella aerator based on dimensional analysis," *Journal of Chemical Engineering of Japan*, vol. 52, no. 4, pp. 369–376, 2019.
- [15] J. Ming, L. Dong, and H. Liu, "Influence of blade shape on performance in inverse umbrella aerator," *Paiguan Jixie Gongcheng Xuebao/Journal of Drainage and Irrigation Machinery Engineering*, vol. 36, no. 2, pp. 104–110, 2018.
- [16] P. Xing, Z. Jing, Y. Yin, and X. Jie, "Finite element analysis and optimization design of inverted umbrella aerator," *Computer simulation*, vol. 27, no. 6, pp. 372–376, 2010.
- [17] P. Xing and B. Qiu, "The Oxidation Ditch Flow Field Analysis Pushed by the New Type Surface Inverted Umbrella Aerator," in *Proceedings of the International Conference on Intelligent System Design and Engineering Applications;ISDEA*, Hong Kong, China, January 2013.
- [18] Y. M. Lau, N. G. Deen, and J. A. M. Kuipers, "Development of an image measurement technique for size distribution in dense bubbly flows," *Chemical Engineering Science*, vol. 94, no. 5, pp. 20–29, 2013.
- [19] M. Honkanen, H. Eloranta, and P. Saarenrinne, "Digital imaging measurement of dense multiphase flows in industrial processes," *Flow Measurement and Instrumentation*, vol. 21, no. 1, pp. 25–32, 2010.
- [20] R. Qiu, R. Zhu, and H. Xu, "Image segmentation algorithm based on improved watershed algorithm," *Journal of Jilin University (SCIENCE EDITION)*, vol. 3, 2017.